CHAPTER 4

$BiFeO_3/CH_3NH_3PbI_3$ Inorganic-Hybrid Organic Perovskites Heterojunction Based Wideband Photodetector*

Contents

4.1 Introduction 82

4.2 Experimental Details 83

4.2.1 Materials Synthesis 83

4.2.2 Device Fabrication 85

4.2.2.1 Substrate Cleaning 85

4.2.2.2 Thin Fim Deposition 85

4.3 Results and Discussion 86

4.3.1 Thin Film Characterizations 86

4.3.2 Electrical Characterizations 92

4.3.3 Optical Characterizations 97

4.4 Conclusion 101

*Part of this work has been published as:

1. ***Rishibrind Kumar Upadhyay et al.,*** "$BiFeO_3/CH_3NH_3PbI_3$ Perovskite Heterojunction Based Near-Infrared Photodetector, "***IEEE Electron Device Letters***, vol. 40, no. 12, pp. 1961-1964, Dec. 2019.

CHAPTER 4

$BiFeO_3/CH_3NH_3PbI_3$ Inorganic-Hybrid Organic Perovskites Heterojunction Based Wideband Photodetector

4.1 Introduction

The literature survey in Chapter-1 shows that perovskites have not been explored significantly for heterojunction-based photodetectors. Spina *et al.* [136] investigated the light intensity-dependent photo-response of a $CH_3NH_3PbI_3/CH_3NH_3SnI_3$ heterostructure photodiode. Some researchers have used metal oxides (e.g. TiO_2 and SnO_2) and $BiFeO_3$ as n-type semiconductors in organic-inorganic perovskites-based heterojunction devices [137]-[139]. The hybrid perovskites act as efficient light-absorbing material in these heterostructure based photodetectors. Etgar *et al.* [140] fabricated the first $CH_3NH_3PbI_3/TiO_2$ heterostructure based photovoltaic device where $CH_3NH_3PbI_3$ served the purpose of both the active layer and HTL simultaneously. However, the requirement of high-temperature annealing, presence of oxygen vacancies/impurities in metal oxides, and poor morphology along with poor crystallinity of $CH_3NH_3PbI_3$ films grown on metal oxides are the major constraints for achieving good quality of hybrid perovskite/metal oxide heterojunction-based photodiodes [141], [142]. Further, the wide absorption spectrum of the $CH_3NH_3PbI_3$ perovskite makes it difficult to fabricate a photodetector with a spectrum selective photo-response [143]. For improving the spectrum selective responsivity in the $CH_3NH_3PbI_3$ based photodetectors, $BiFeO_3$ is used for an efficient optical filter [144] as well as an electron transport layer [138] in the perovskite-based heterojunctions. Since $CH_3NH_3PbI_3$ and $BiFeO_3$ are both perovskite materials, it is also expected that the quality of $CH_3NH_3PbI_3/BiFeO_3$ heterojunction will be better than that

of the $CH_3NH_3PbI_3$/metal-oxide heterojunctions. Therefore, after exploring the inorganic perovskite $BiFeO_3$ for white light detection in Chapter-2 and hybrid perovskite $CH_3NH_3PbI_3$ for wideband photodetection application in Chapter-3, the present chapter has been devoted to investigate the performance characteristics of the $BiFeO_3$/ $CH_3NH_3PbI_3$ heterostructure for wideband photodetection application covering both the visible and NIR regions.

In this Chapter, a $CH_3NH_3PbI_3/BiFeO_3$ heterojunction photodetector fabricated on an ITO substrate is proposed where $BiFeO_3$ serves as an optical filter-cum-ETL in the device. The combined effects of the ITO substrate and $BiFeO_3$ based ETL are used to improve the responsivity of the proposed photodetector. The electrical and optical responses of the proposed perovskite heterojunction have been investigated for wavelengths over 400-900 nm. The layout of the present chapter is given in the following.

Section 4.2 presents the experimental details of the $BiFeO_3/CH_3NH_3PbI_3$ heterojunction photodetector. The results and discussions related to the thin film characterizations and photo-response measurements are discussed in section 4.3. Finally, section 4.4 is used to summarize the major observations of this chapter.

4.1 Experimental Details

4.1.1 Materials Synthesis

All the chemicals are used as received from Sigma-Aldrich and Merck Chemicals without any further purifications. The inorganic perovskite $BiFeO_3$ (BFO) NPs were synthesized by the solid-state route using a mortar and pestle grinding by hand for more than 50 hours. In this process, the (3.72375 gm) powders of bismuth oxide (Bi_2O_3) and (1.2762 gm) iron (III) oxide (Fe_2O_3) were first mixed in a stoichiometric ratio. A few drops of ethanol were added to it for better mixing [41]. Finally, the calcinated BFO NPs

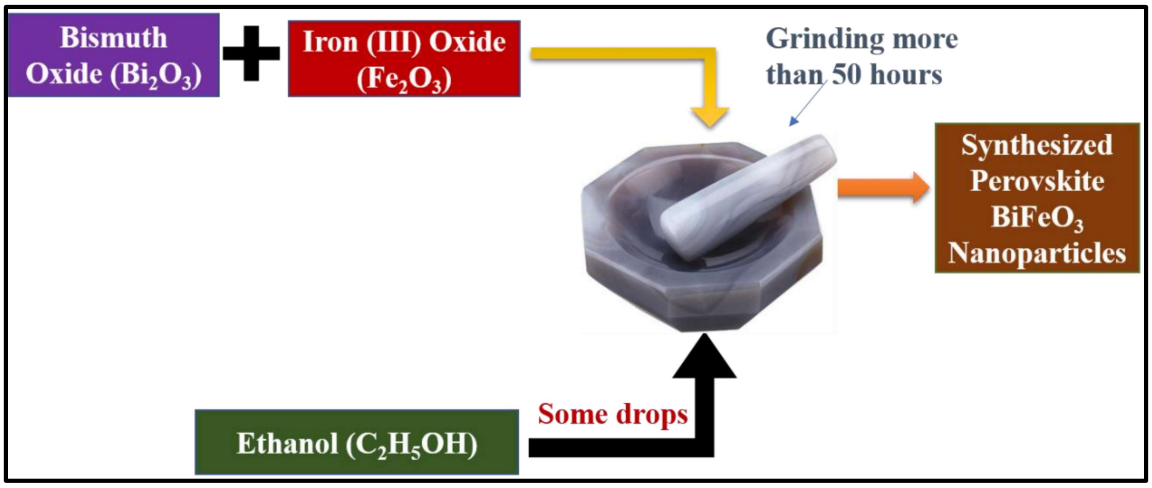

Figure 4.1: Synthesis of the perovskite $BiFeO_3$ nanoparticles.

were obtained by drying the resultant mixture in two steps: first at 600°C for 1 hour and then 800°C for 2 hour [42]. A schematic representation of the synthesis of the $BiFeO_3$ is shown in Figure 4.1.

The hybrid perovskite $CH_3NH_3PbI_3$ NPs were synthesized by the sol-gel route. A precursor solution of hybrid $CH_3NH_3PbI_3$ was composed using an equimolar (1:1) mixture of (0.15897 gm) methylammonium iodide (CH_3NH_3I) and (0.46101 gm) lead iodide (PbI_2). The solvent of (CH_3NH_3I) and lead iodide (PbI_2) solution was (1 ml each) N, N-dimethylformamide anhydrous (DMF) and put this solution for stirring at room temperature for 24 hours [43], [44]. Finally, the yellowish colour solution of hybrid perovskite $CH_3NH_3PbI_3$ is obtained. A schematic representation of the synthesis of the hybrid perovskite $CH_3NH_3PbI_3$ nanoparticles is shown in Figure 4.2.

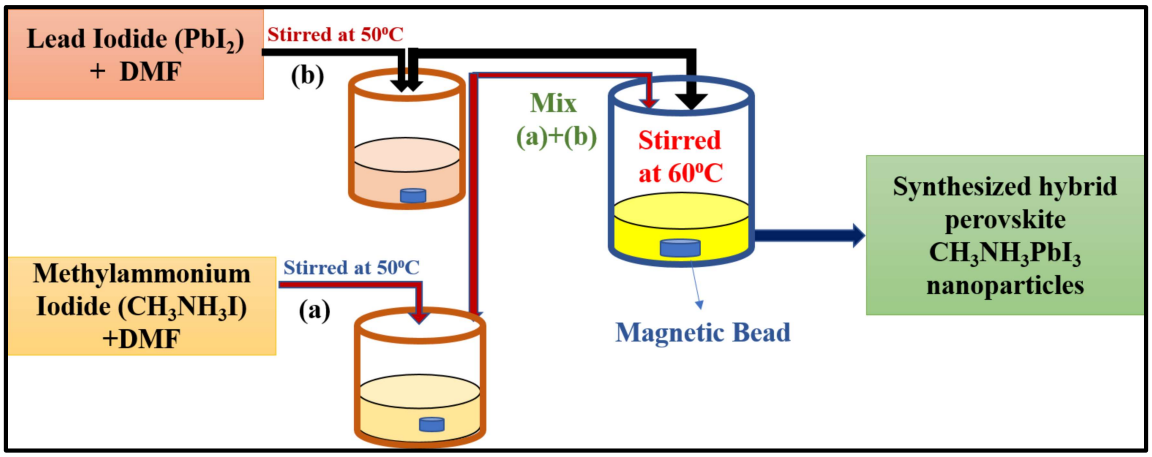

Figure 4.2: Synthesis of the hybrid perovskite $CH_3NH_3PbI_3$ nanoparticles.

4.2.2 Device Fabrication

In this section, we are discussing the substrate cleaning process, thin-film deposition in detail.

4.2.2.1 Substrate Cleaning

In the present work indium doped tin oxide (ITO) coated glass substrates with thickness ~1.1 mm and resistivity ~15-20 (ohm.cm) was cut into small regular square-shaped (15×15 mm^2) using a diamond cutter. The small ITO substrate piece was cleaned thoroughly. At first, ITO coated glass substrates were sequentially cleaned in an ultrasonic cleaning bath in a 5% soap solution to remove dust particles for 15 min., then deionized (DI) water with a resistivity of ~18 (MΩ.cm) to get rid of chemical residues for 15 min., then acetone (C_3H_6O) to remove the organic remnants/contaminants from the substrate for 15 min., at last, cleaned by isopropanol (C_3H_8O) for 10 minutes to remove organic residues left on substrate. Then, the substrates were treated by plasma cleaning in the presence of oxygen and argon for 15 minutes to increase the hydrophilicity of ITO coated glass substrate.

4.2.2.2 Thin Film Deposition

In the first deposition step, a thin film of $BiFeO_3$ nanoparticles dispersed in ethanol was deposited on the as cleaned ITO coated glass substrate by the spin coating unit (TSE, Model SPM-150LC, Germany) and then the film is annealed in an ambient environment at 300°C for 1 hour. In the second step, hybrid $CH_3NH_3PbI_3$ solution is deposited multiple times on the $BiFeO_3$ nanoparticles thin film by using the spin coating to obtain a total thickness of ~250 nm. The $CH_3NH_3PbI_3$ film is dried at 70°C for 15 minutes after every step. Later, the perovskite thin film is annealed at 120°C for 20 minutes under ambient air conditions on a hot plate. For contact electrode formation, Ag (99.99%) metal dots of ~2 mm diameter (device area 0.0314 cm^2) and ~100 nm thickness were fabricated on the

$CH_3NH_3PbI_3$ film by thermal evaporation unit (Model No. FL400, SMART COAT 3.0 A, Hind High Vacuum India) with the shadow mask technique. The vacuum level was maintained in the range of 10^{-6} mbar with a deposition rate of 0.02 Å/s in the thermal evaporation unit. The thicknesses of different layers of the device were measured using the optical spectrometer commonly known as F20-UV, thin-film analyzer (Model No. SDT2, Filmetrics USA) instrument. A schematic block diagram of the fabricated steps used for the fabrication of the photodetector is shown in Figure 4.3.

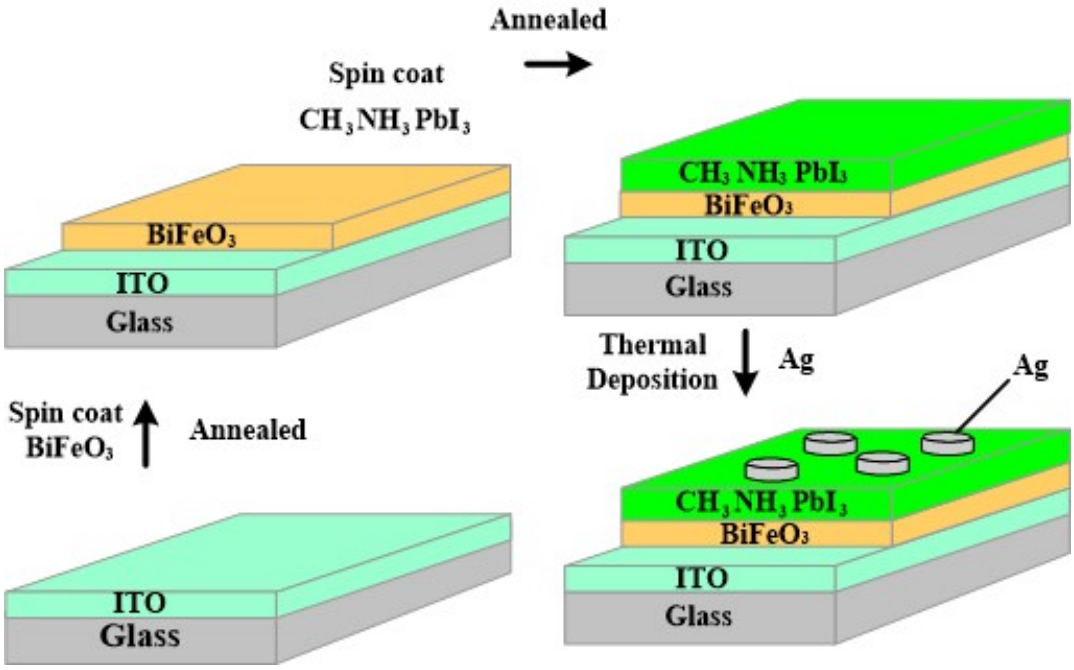

Figure 4.3: Schematic block diagram of the fabricated steps used for fabrication of photodetector device.

4.3 Results and Discussion

In this section, structural, optical and electrical characterization of $BiFeO_3/CH_3NH_3PbI_3$ perovskite-based device, are discussed.

4.3.1 Thin Film Characterization

(a) Crystallographic orientation by XRD Analysis

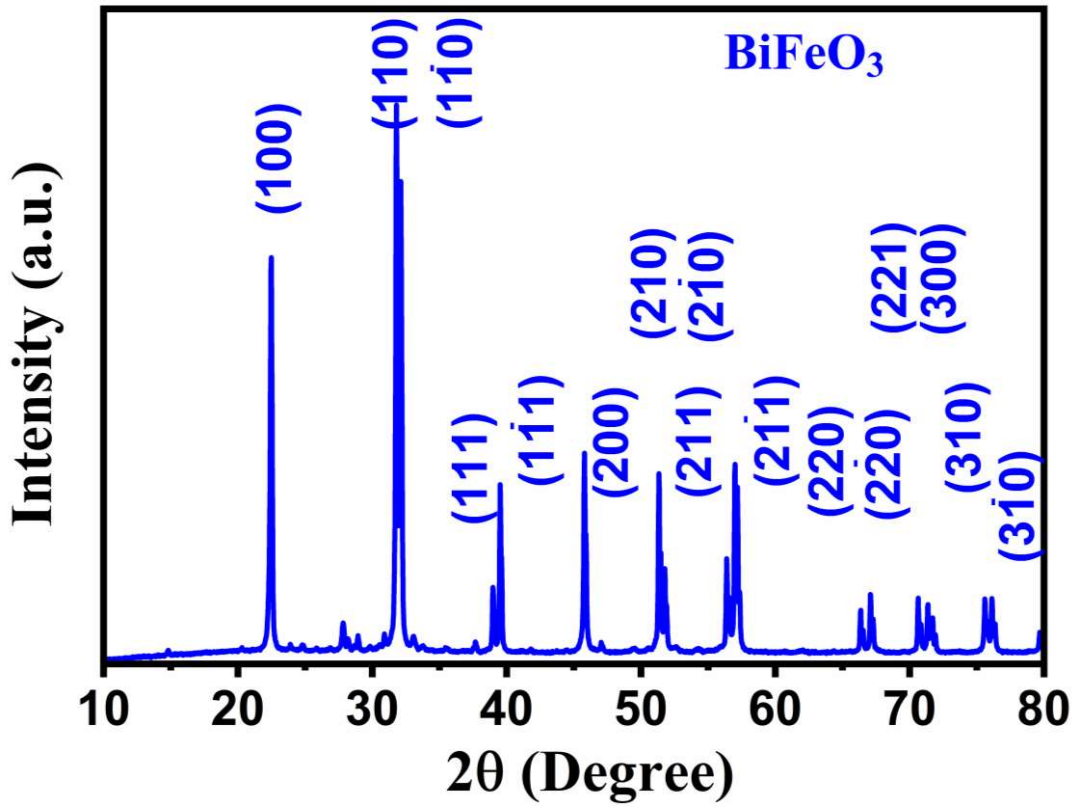

Figure 4.4: XRD peaks of the $BiFeO_3$ nanoparticles coated on the glass substrate using X-ray diffraction (RIGAKU-Smart XDMAX, PC-20, 18-Kw Cu rotating anode, Rigaku, Tokyo) at room temperature.

The crystalline structure of inorganic $BiFeO_3$ thin film and hybrid perovskite $CH_3NH_3PbI_3$ nanoparticles thin films have been investigated by X-ray diffraction (RIGAKU-Smart XDMAX, PC-20, 18-Kw Cu rotating anode, Rigaku, Tokyo) at room temperature. Major diffraction peaks observed in XRD spectra of $BiFeO_3$ samples at 22.48°, 31.8°, 39.52°, 47.04°, 51.34°, 57.00° are assigned to (100), (110), (111), (200), (210) and (211) planes, respectively. The obtained diffraction peaks are well matched to the rhombohedral structure of $BiFeO_3$ with space group $R3m$ (JCPDS card number 74-2016) [42], [121]. The measured XRD spectra of $BiFeO_3$ NPs has been shown in Figure 4.4. The thin film of $CH_3NH_3PbI_3$ is also investigated using XRD in continuous scan mode from XRD angle (2θ, 10 degrees to 60 degrees) and preferred orientations at 14.48°, 28.93°, 32.20°, 40.86°, 43.51° are observed, with these assigned to the (110), (220), (310), (224) and (330) planes, respectively of $CH_3NH_3PbI_3$ perovskite tetragonal structure and

orientations at 20.06°, 24.05°, 24.64°, 35.50°, 51.25°and 52.60° assigned to the minor facet (200), (211), (202), (312), (404), (226) planes, respectively [132], which indicated that perovskite film is of high phase purity. The measured XRD spectra of $CH_3NH_3PbI_3$ NPs has been shown in Figure 4.5.

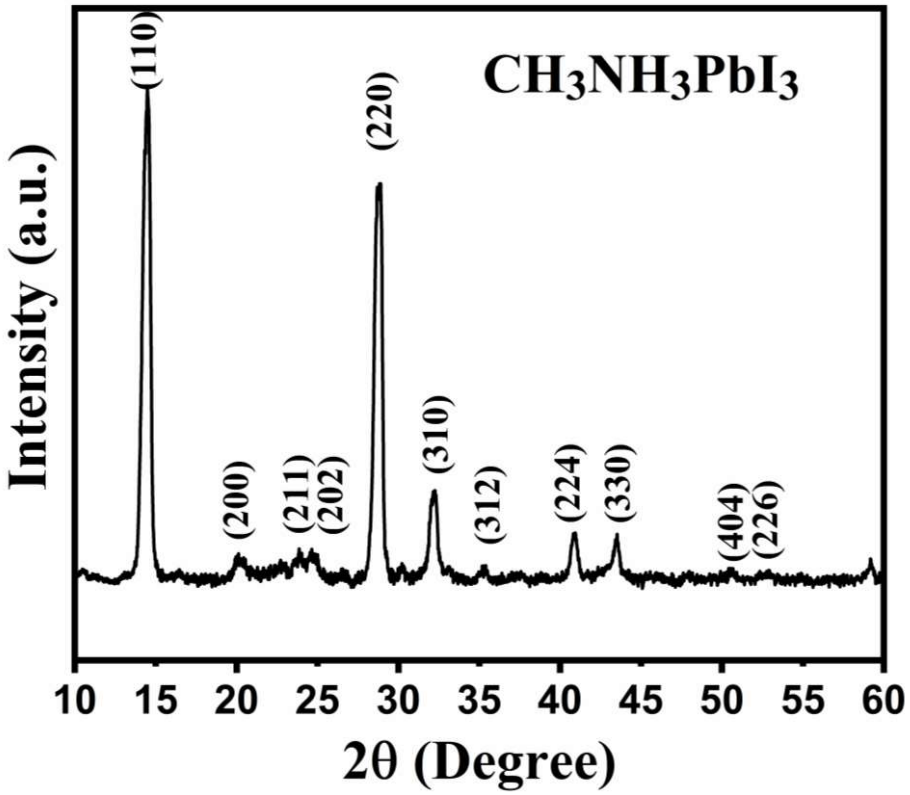

Figure 4.5: XRD pattern of the perovskite $CH_3NH_3PbI_3$ thin film deposited on the glass substrate using X-ray diffraction (RIGAKU-Smart XDMAX, PC-20, 18-Kw Cu rotating anode, Rigaku, Tokyo) at room temperature.

(b) Surface Morphology

The surface morphology of the synthesized inorganic $BiFeO_3$ and hybrid $CH_3NH_3PbI_3$ perovskites are investigated using a high-resolution scanning electron microscope (HRSEM, Nova Nano SEM 450, USA). The obtained HRSEM image of $BiFeO_3$ thin film is shown in Figure 4.6. (Inset HRSEM image of $BiFeO_3$ nano-powder). It can be seen from the inset HRSEM image the synthesized $BiFeO_3$ nano-powder has uniformly grown high-density nanoparticles in the range of 50-80 nm diameter and some

agglomerated large particles. Further, as-deposited $BiFeO_3$ thin film using $BiFeO_3$ nano-powder has a uniform distribution of the particle for the formation of continuous and regular thin film as shown in Figure 4.6. On the other hand, the $CH_3NH_3PbI_3$ film has also a uniform distribution of nanoparticles in the range of 40-50 nm diameter as shown in Figure 4.7. The small particle sizes of $BiFeO_3$ and $CH_3NH_3PbI_3$ films enhance the optoelectronic performance due to the enhanced quantum confinement effect [134].

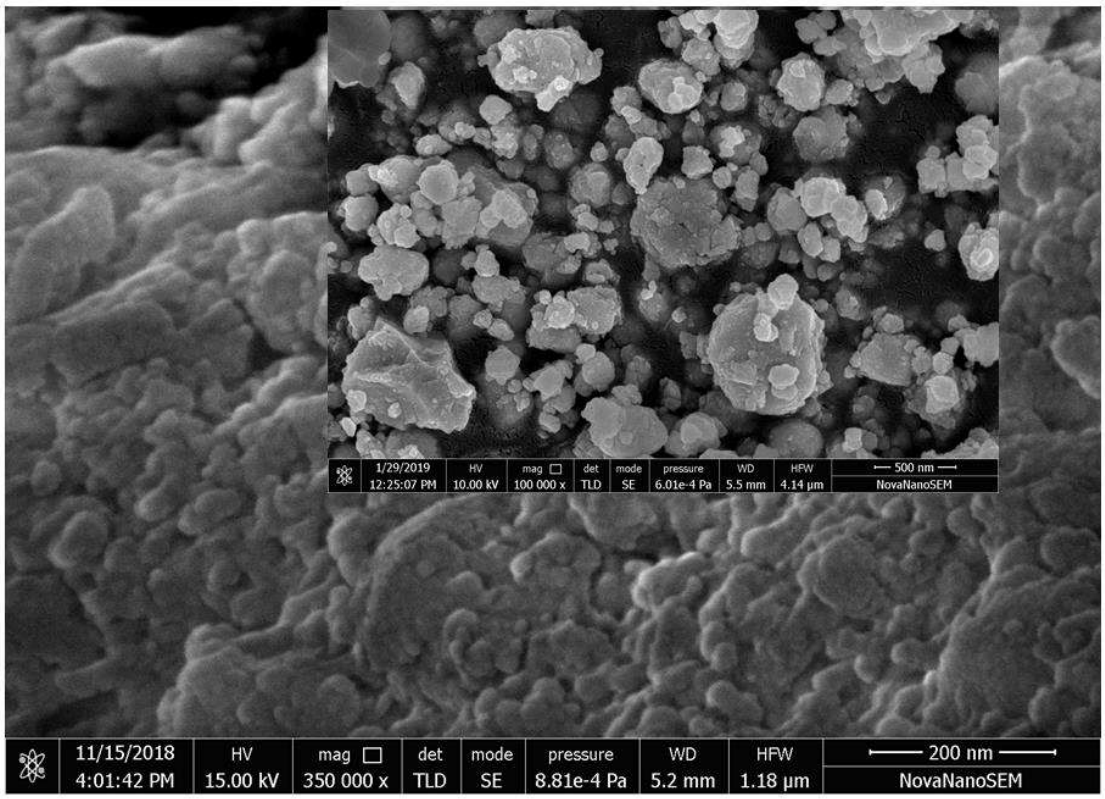

Figure 4.6: HRSEM image of the $BiFeO_3$ thin film on the glass substrate (Inset HRSEM image of $BiFeO_3$ nano-powder) using high-resolution scanning electron microscope (HRSEM, Nova Nano SEM 450, USA).

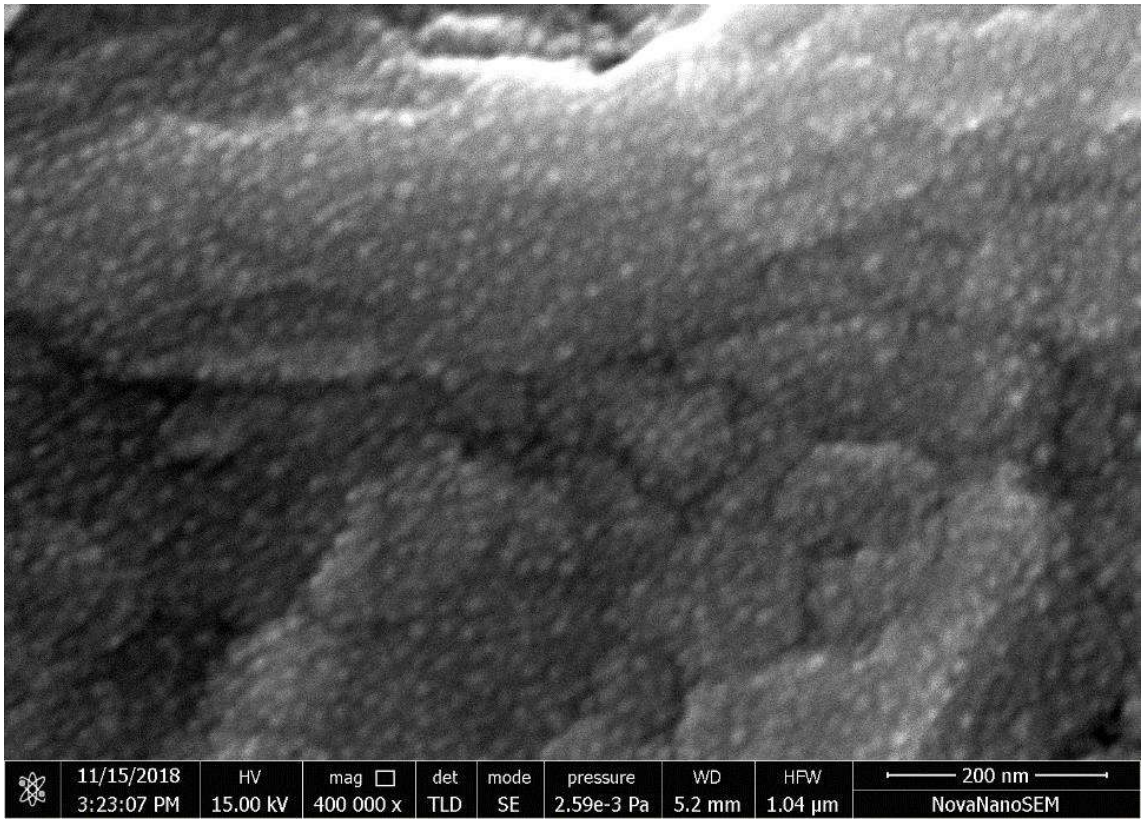

Figure 4.7: HRSEM image of the perovskite $CH_3NH_3PbI_3$ thin film on the glass substrate using high-resolution scanning electron microscope (HRSEM, Nova Nano SEM 450, USA).

(c) UV-Vis Analysis

Ultraviolet-Visible (UV-Vis) spectroscopy (V-770 from JASCO, Japan) talks about absorption or reflectance spectroscopy which is typically used for estimation bandgap of materials and optical absorbance of materials. To determine the bandgap of (E_g) of hybrid perovskite $CH_3NH_3PbI_3$ and inorganic perovskites $BiFeO_3$ thin film under consideration, we have plotted $(\alpha h\nu)^{1/n}$ versus photon energy $h\nu$ as shown in Figure 4.9. According to Beer–Lambert's equation, the absorption coefficient α of sample material is given by following relation [122]:

$$\alpha = 2.303 Abs \frac{(\lambda)}{t} \qquad \text{.....(4.1)}$$

where t is the thickness of thin film and absorbance coefficient Abs (λ) of a thin film is measured from the absorbance curve, experimentally measured by Ultraviolet-Visible

(UV-Vis) spectroscopy. At room temperature, the measured Abs (λ) of the hybrid perovskite $CH_3NH_3PbI_3$ and inorganic perovskites $BiFeO_3$ thin film on the glass substrate is displayed in Figure 4.8. It is observed that the $BiFeO_3$ layer blocks (i.e. absorbs) the lower wavelengths and transmits efficiently the NIR wavelengths of the incident light to the active layer.

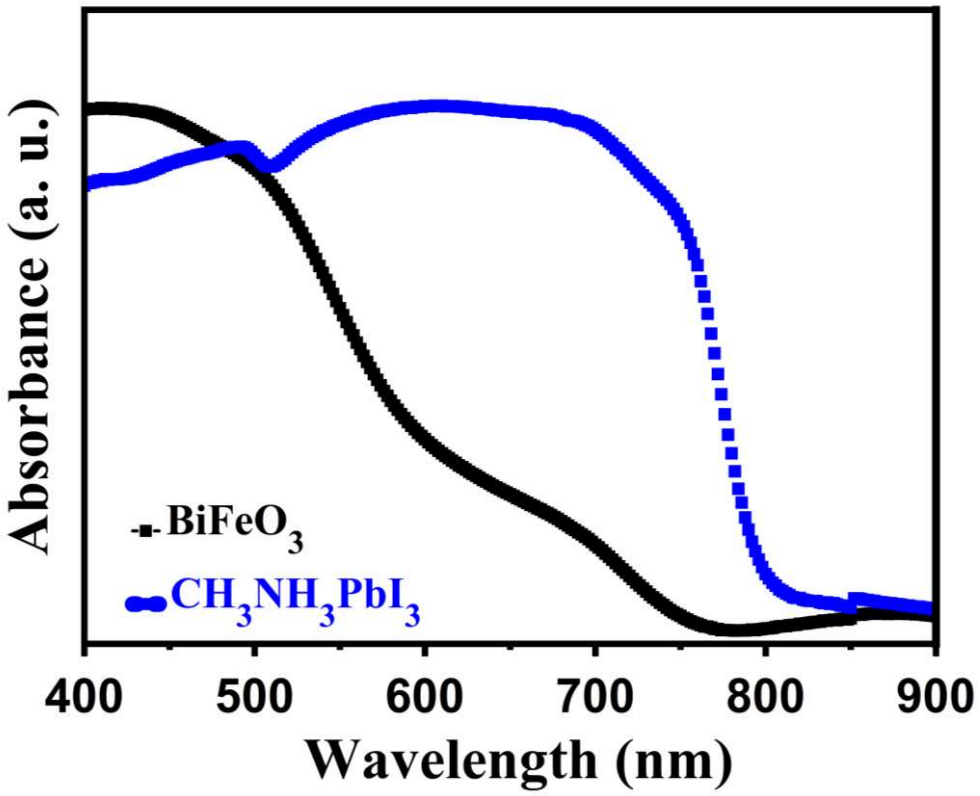

Figure 4.8: Absorbance spectra of the $BiFeO_3$ nanoparticles and $CH_3NH_3PbI_3$ thin film deposited on the glass substrate using (UV-Vis) spectroscopy (V-770 from JASCO, Japan).

Thus, it works as an optical filter-cum-hole blocking layer to enable the detection of NIR light with high selectivity of the photodetector.

Further, the absorption coefficient as a function of the energy of a photon is expressed by Tauc relation [50], [122]:

$$(\alpha h\nu)^{1/n} = \beta(h\nu - E_g) \qquad \text{.....(4.2)}$$

where β, α, h, ν, Eg and n are the constants representing the band tailing parameter, absorption coefficients, Plank constant, light frequency, optical band gap, and empirical constant, respectively. The value of n depends on material properties, which are taken as 1/2, 2, 3/2, and 3 for direct allowed, indirect allowed, direct forbidden, and indirect forbidden transitions, respectively.

Hence by extrapolating the linear part of $(\alpha h\nu)^{1/n} = \beta(h\nu - E_g) = 0$ (as displayed in Figure 4.9) the estimated optical band gap of the perovskites, $BiFeO_3$ nanoparticles, and $CH_3NH_3PbI_3$ thin film are ~2.02 eV and ~1.49 eV, respectively.

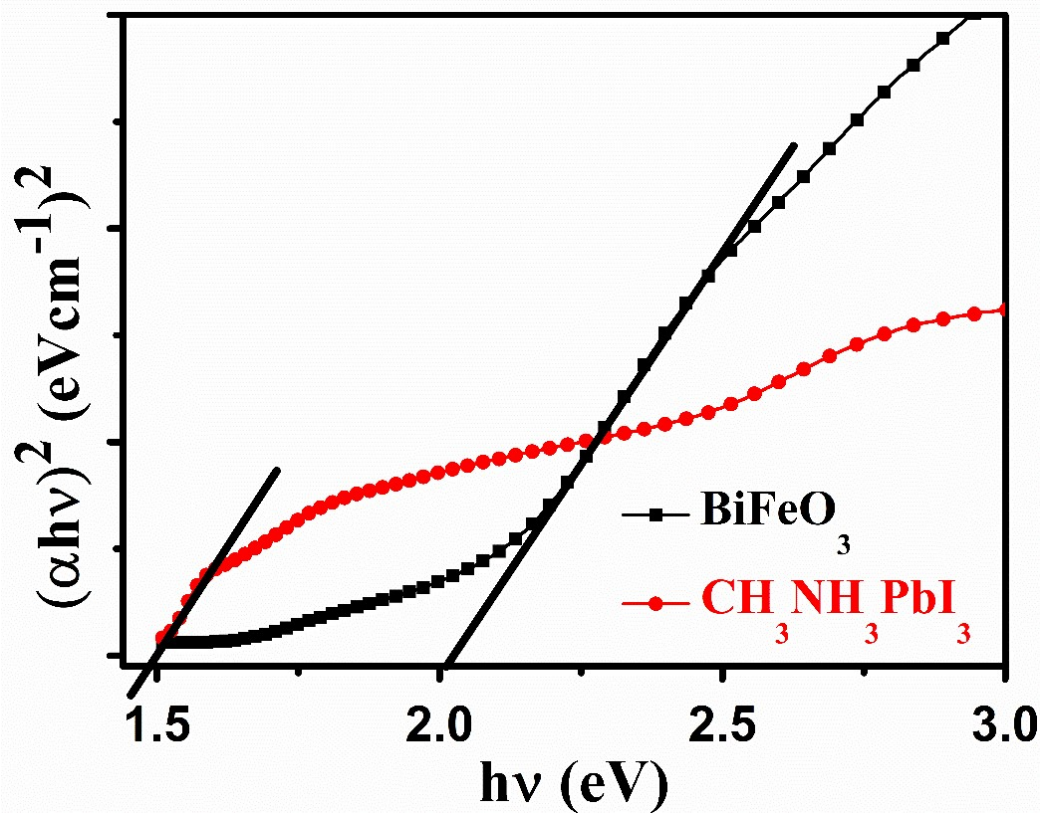

Figure 4.9: Tauc plot of the $BiFeO_3$ nanoparticles and $CH_3NH_3PbI_3$ thin film deposited on the glass substrate for bandgap calculation using (UV-Vis) spectroscopy (V-770 from JASCO, Japan).

4.4.2 Electrical Characterizations

After investigating the thin film properties, we now examined the room temperature electrical characterizations via capacitance-voltage (*C-V*) characteristics and current-

voltage *(I–V)* characteristics measurements for the fabricated device structure.

(a) capacitance-voltage (C-V) characteristics

Capacitance-voltage (*C-V*) characteristics are performed at 1000 Hz frequency using a semiconductor parameter analyzer (B1500A from Keysight, USA) for ITO/$BiFeO_3$/$CH_3NH_3PbI_3$/Ag device at room temperature. The *C-V* measurement has been done to include only the depletion layer capacitance by avoiding the excess capacitance due to interface states at low frequencies [50], [123]. The existence of a capacitance confirms the formation of a depletion region at the junction of the heterojunction device. Capacitance-voltage *C-V* characteristics of the fabricated heterostructure device is shown in Figure 4.10.

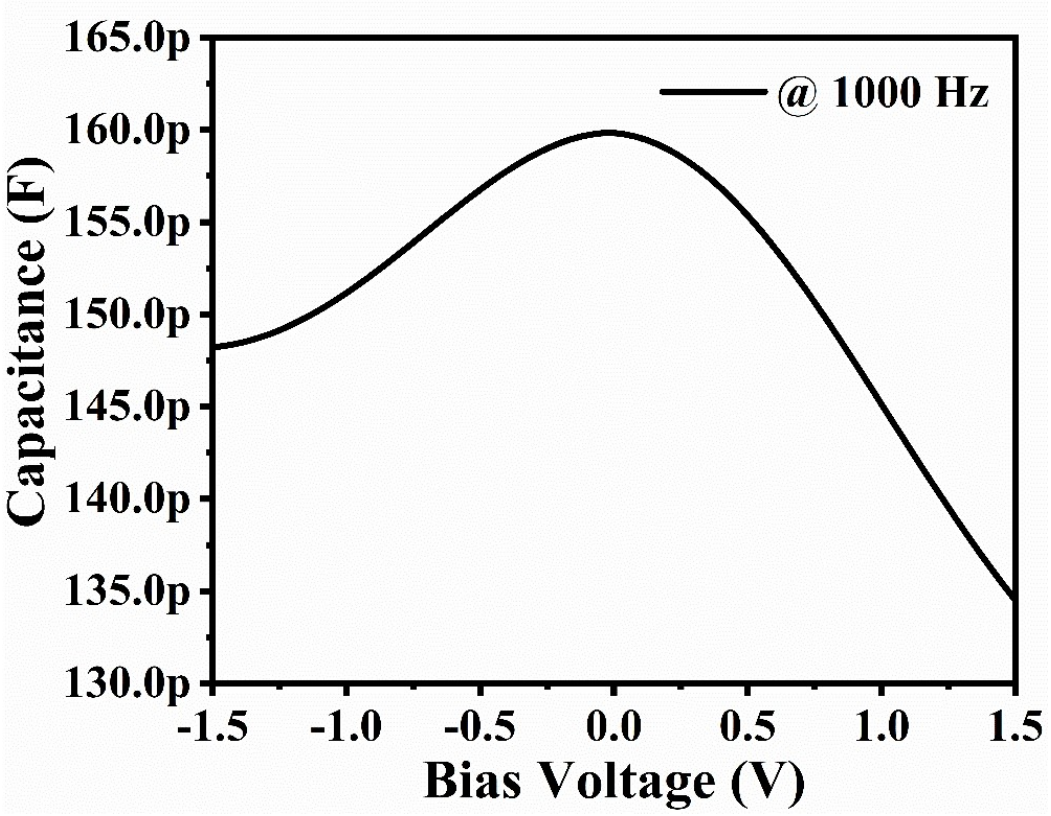

Figure 4.10: Capacitance-voltage *(C-V)* characteristics of the fabricated heterostructure device at 1000 Hz frequency using a semiconductor parameter analyzer (B1500A from Keysight, USA).

(b) Energy Band Diagram

Here, we discussed the photodetection mechanism for fabricated photodetector

devices. Note that the operation of ITO/$BiFeO_3$/$CH_3NH_3PbI_3$/Ag heterojunction device under light illumination involves three steps:

(i) The generation of charge carrier by incident light.

(ii) The separation and transport of charge carrier by internal field in the depletion region.

(iii) Extraction of charge carrier as terminal current to provide output signal [50], [126].

The operation of the ITO/$BiFeO_3$/$CH_3NH_3PbI_3$/Ag heterojunction photodetector under consideration has been demonstrated in Figure 4.11 through an energy band diagram of a fabricated device under light illumination and reverse bias operation. The fabricated photodetector device is illuminated from (Glass/ITO Side) to gain 100% illumination area. Note that the major portion of the light will be reflected back to open space from the metal surface if the device is illuminated from the metal contact side The $BiFeO_3$ NPs layer used in the device performs two major operations.

(i) The $BiFeO_3$ NPs layer is used as an electron device layer (ETL) as well as n-type material in the device. The excess photogenerated electron-hole pairs (EHPs) in the active region (i.e. depletion region of $CH_3NH_3PbI_3$) are drifted out to the inherent electric field of the depletion region. The photogenerated electron moves toward the $BiFeO_3$ NPs layer while the hole moves toward the Ag electrode.

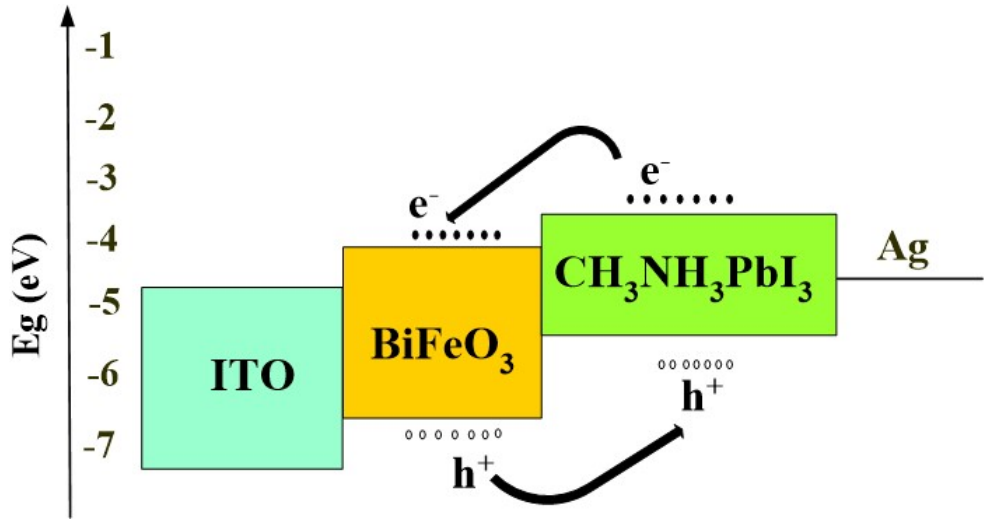

Figure 4.11: Schematic energy band diagram of the proposed heterojunction photodetector.

(ii) The $BiFeO_3$ NPs layer deposited over ITO substrate also acts as an optical filter for photodetection operation. Figure 4.8 absorption spectra of $BiFeO_3$ nanoparticles and $CH_3NH_3PbI_3$ deposited on a glass substrate shows the absorption range of $BiFeO_3$ and $CH_3NH_3PbI_3$ thin film. It is observed that the $BiFeO_3$ layer blocks (i.e. absorbs) the lower wavelengths and transmits efficiently the NIR wavelengths of the incident light to the active layer. Thus, it works as an optical filter-cum-hole blocking layer to enable the detection of NIR light with high selectivity of the photodetector.

(c) current-voltage (I-V) characteristics

The measured current-voltage *(I–V)* characteristics of the $ITO/BiFeO_3/CH_3NH_3PbI_3/Ag$ heterojunction have been shown in Figure 4.12. The current-voltage *(I–V)* characteristics are measured at room temperature and in -2 V to 2 V bias voltage range by using a semiconductor parameter analyzer (B1500A from Keysight, USA) under dark and light illumination (monochromatic light of 800 nm with an optical power of ~1.4 μW) condition. Under the reverse bias of 2 V, the dark current of 0.057 μA and the light current of 0.35 μA is obtained. For reverse saturation current calculation, we compare the current-voltage *(ln I–V)* characteristics as shown in Figure

4.13. A reverse saturation current of ~9.8 $x10^{-10}$ A is calculated from the standard diode equation in the dark condition [50].

$$I = I_0 \left\{ exp\left(qV/\eta kT\right) - 1 \right\} \quad \ldots\ldots\ldots\ldots (4.3)$$

where q is the electronic charge, η is the ideality factor of the heterojunction, V is the bias voltage, I_0 is the reverse saturation current, and T is the absolute temperature.

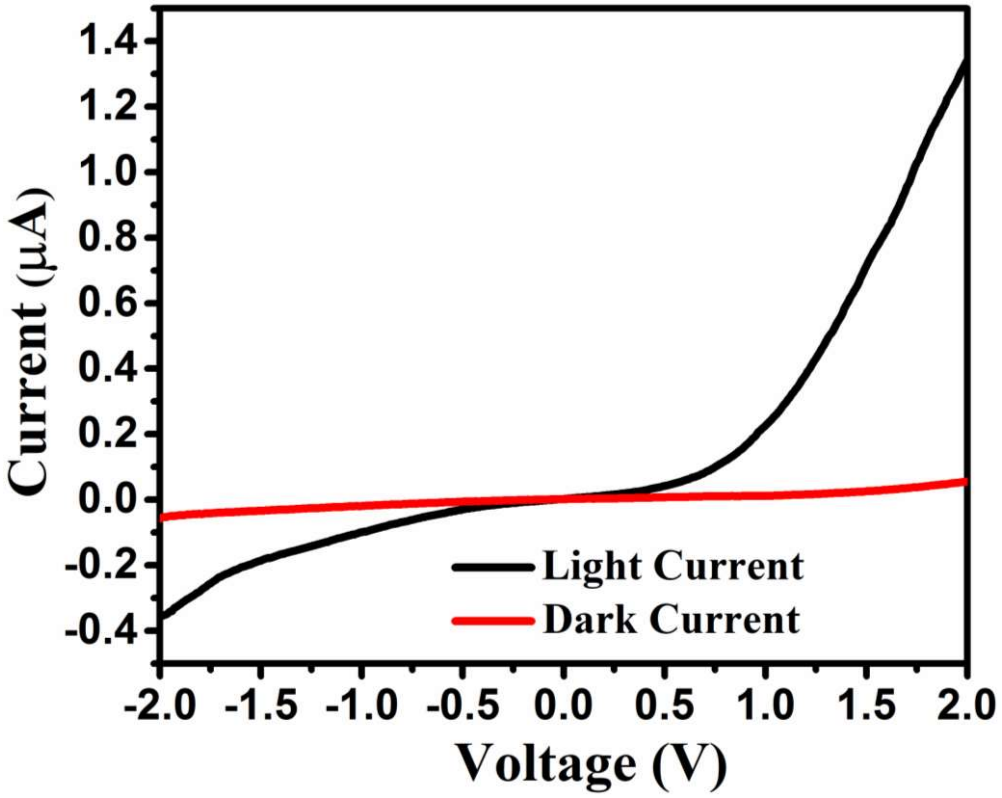

Figure 4.12: Current-voltage (*I-V*) characteristics of the proposed heterojunction photodetector at room temperature and in -2 V to 2 V bias voltage range by using a semiconductor parameter analyzer (B1500A from Keysight, USA) under dark and light illumination (monochromatic light of 800 nm with an optical power of ~1.4 μW) condition.

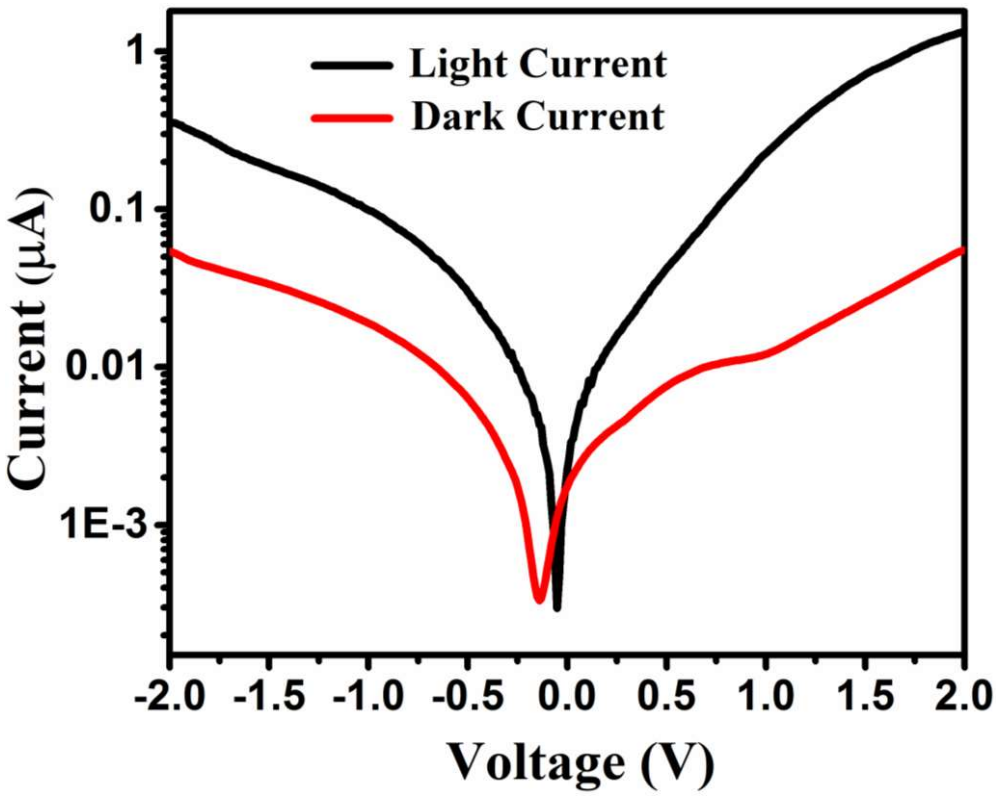

Figure 4.13: Logarithmic current-voltage *(I-V)* of the proposed heterojunction photodetector at room temperature and in -2 V to 2 V bias voltage range by using a semiconductor parameter analyzer (B1500A from Keysight, USA) under dark and light illumination (monochromatic light of 800 nm with an optical power of ~1.4 μW) condition.

4.4.3 Optical Characterizations

The wavelength (λ) dependent optical power density P_{opt} (λ) of the incident monochromatic light is measured by a power meter (PM100D, Thorlabs). The responsivity and detectivity of the proposed photodetector are measured over 400 to 900 nm obtained from a monochromator (SP2150i from Princeton Instruments, USA) along with a halogen light source using the following relation:

$$R(\lambda) = I(\lambda, V) / AP_{opt}(\lambda) \quad \text{..... (4.4)}$$

$$D(\lambda, V) = R(\lambda) \times [RA(\lambda, V)/4kT]^{1/2} \quad \text{..... (4.5)}$$

where I (λ, V) = (I_{light} - I_{dark}) is the photocurrent density of the detector. I_{light} and I_{dark} denote the current under light exposure and dark conditions, respectively. A and P_{opt} (λ)

denote the effective exposed irradiation area of the heterojunction and optical power density, respectively. The wavelength (λ) dependent optical power density P_{opt} (λ) of the incident light from a monochromator setup is measured using a power meter (PM100D, Thorlabs).

Here, RA (λ, V) is the resistance–area product for the fabricated heterojunction given by:

$$RA(\lambda, V) = (d J(\lambda, V)/dV)^{-1} \quad \ldots\ldots\ldots\ldots\ldots\ldots (4.6)$$

Figure 4.14 gives a very promising responsivity of ~2 A/W and detectivity of ~7.8×10^{12} $cmHz^{1/2}/W$ for the heterojunction photodetector at a bias voltage -2V, 800 nm and ~44.4 $\mu W/cm^2$ incident optical power density.

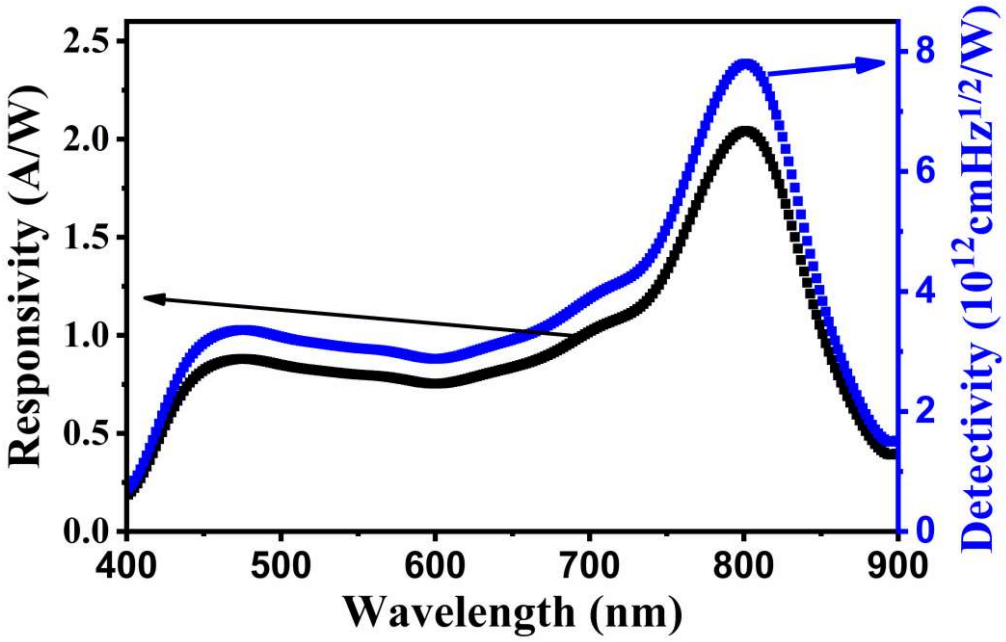

Figure 4.14: Responsivity and detectivity of the fabricated photodetector device against wavelength in the range of 400-900 nm from a monochromator (SP2150i from Princeton Instruments, USA) along with a halogen light source.

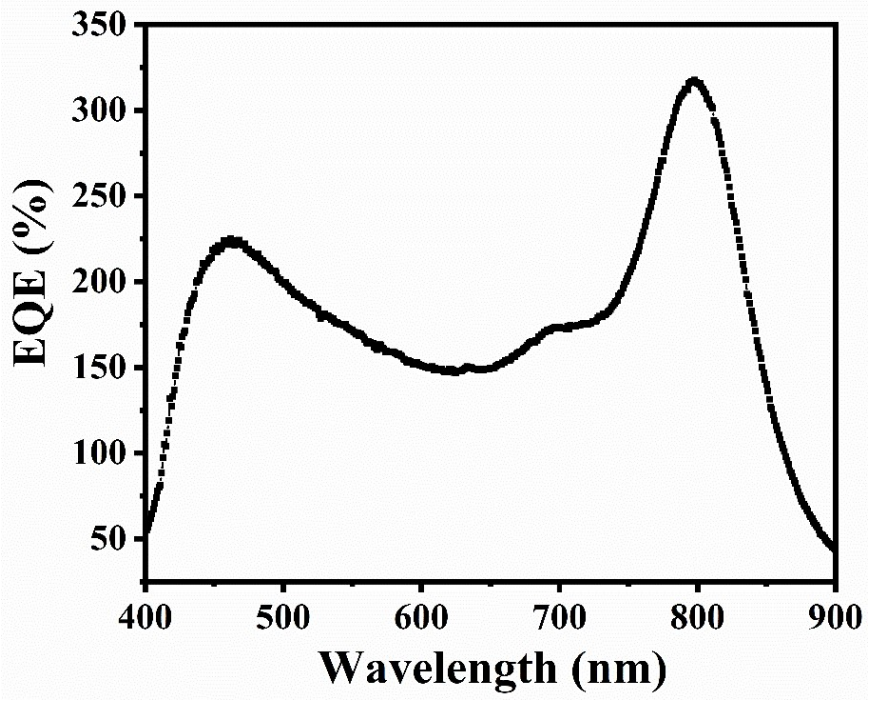

Figure 4.15: External quantum efficiency (EQE) of the fabricated photodetector device against wavelength in the range of 400-900 nm from a monochromator (SP2150i from Princeton Instruments, USA) along with a halogen light source.

With the help of the responsivity of the proposed photodetector we can easily calculate the external quantum efficiency (EQE) of the proposed photodetector by using the following relation:

$$EQE(\%) = 1240 \frac{R(\lambda)}{\lambda} * 100 \qquad \text{..... (4.7)}$$

Figure 4.15 shows the external quantum efficiency (EQE) of the proposed photodetector measured over 400 to 900 nm. The maximum value of ~310% external quantum efficiency (EQE) of the proposed photodetector is obtained at 800 nm at an applied bias voltage of -2V.

Further, the repeatability of the results and response speed of the heterojunction photodetector are investigated using transient response measurement. For repeatability of the results, we have used a digital multimeter (Agilent, 34410 A) and monochromator light Source with an on-off time of 5 s each (power density of ~44.4 $\mu W/cm^2$) at ambient

room temperature (27°C) and biased voltage of -2V. The ON-OFF pulsating is obtained by using an Arduino™ microcontroller and the digital multimeter is controlled by Lab View™. The repeatability and speed characteristics of heterojunction photodetector are shown in Figure 4.16. The characteristics reveal that the response performance of the heterojunction photodetector is repeatable. The speed of the photodetector is measured in terms of rise time and fall time, which are calculated as time elapsed to change the current from 10% to 90% and 90% to 10%, respectively. The rise time and fall time characteristics of the photodetector are shown in Figure 4.17. The rise time and fall time are estimated as 0.74 sec. and 0.088 sec., respectively.

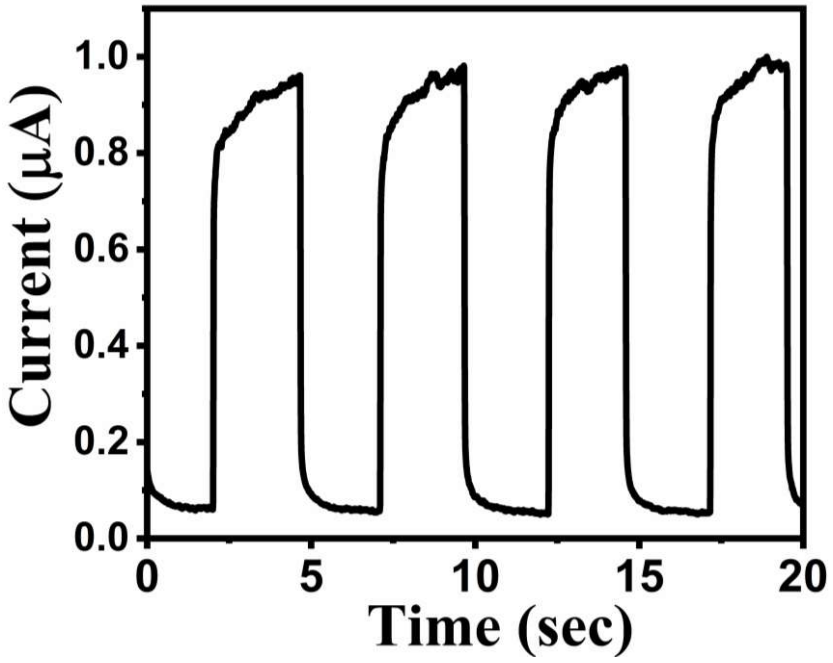

Figure 4.16: Transient photoresponse characteristics of the fabricated photodetector under on-off pulse of monochromatic light of 800 nm with an optical power density of ~44.4 μW/cm^2.

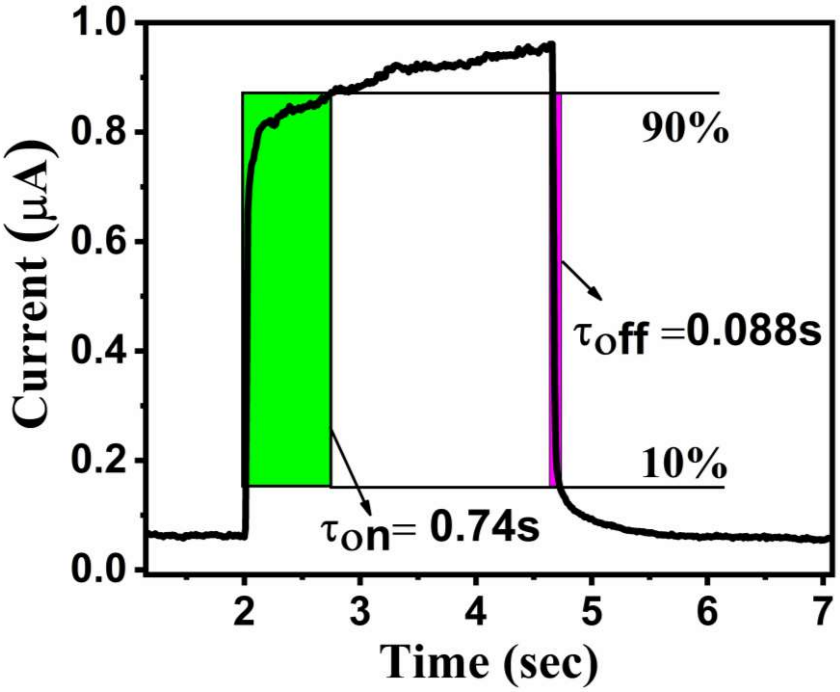

Figure 4.17: Rise time and fall time characteristics of the fabricated photodetector under the illumination of monochromatic light of 800 nm with an optical power density of ~44.4 μW/cm^2.

4.4 Conclusion

This chapter studied the fabrication and characterization of $BiFeO_3/CH_3NH_3PbI_3$ heterojunction based wideband photodetector. The crystalline structure, surface morphology, and optical properties of the films are investigated using XRD, HRSEM, and UV-Visible analysis, respectively. It is found that the $BiFeO_3$ nanoparticles have a rhombohedral crystalline structure, whereas the $CH_3NH_3PbI_3$ thin film is a tetragonal structure with high phase purity. The fabricated heterojunction $ITO/BiFeO_3/CH_3NH_3PbI_3/Ag$ is characterized under dark and monochromatic light illumination (optical power density of ~44.4 μW/cm^2), respectively. The fabricated heterojunction photodetector exhibits a maximum responsivity of ~2 A/W, detectivity of ~7.8x10^{12} cmHz$^{1/2}$/W and external quantum efficiency (EQE) of ~310% at a wavelength of ~800 nm, with rise time and fall time of 0.74 s and 0.088 s, respectively.